




Infrared spectra in amorphous alumina: A combined *ab initio* and experimental studyLuigi Giacomazzi ^{*}*Institute of Materials (IOM), National Research Council of Italy (CNR), c/o SISSA Via Bonomea 265, IT-34136 Trieste, Italy and Materials Research Laboratory, University of Nova Gorica, Vipavska 11c, SI-5270 Ajdovščina, Slovenia*Nikita S. Shcheblanov [†]*Navier, UMR 8205, Ecole des Ponts ParisTech, Université Gustave Eiffel, CNRS, Marne-la-Vallée, France and MSME, UMR 8208, Université Gustave Eiffel, CNRS, Université Paris-Est Créteil, Marne-la-Vallée, France*Mikhail E. Povarnitsyn *Joint Institute for High Temperatures, RAS, 13 Building 2, Izhorskaya Street, Moscow 125412, Russia*Yanbo Li *Institute of Fundamental and Frontier Sciences, University of Electronic Science and Technology of China, Chengdu 610054, China*Andraž Mavrič *Materials Research Laboratory, University of Nova Gorica, Vipavska 11c, SI-5270 Ajdovščina, Slovenia*Barbara Zupančič  and Jože Grdadolnik *Laboratory for Molecular Structural Dynamics, Theory Department, National Institute of Chemistry, 1000 Ljubljana, Slovenia*Alfredo Pasquarello *Chaire de Simulation à l'Echelle Atomique (CSEA), Ecole Fédérale Polytechnique de Lausanne (EPFL), CH-1015 Lausanne, Switzerland*

(Received 17 January 2023; accepted 13 March 2023; published 24 April 2023)

We present a combined study based on the experimental measurements of an infrared (IR) dielectric function and first-principles calculations of IR spectra and the vibrational density of states (VDOS) of amorphous alumina (am- Al_2O_3). In particular, we show that the main features of the imaginary part of the dielectric function $\epsilon_2(\omega)$ at ~ 380 and 630 cm^{-1} are related to the motions of threefold-coordinated oxygen atoms, which are the vast majority of oxygen atoms in am- Al_2O_3 . Our analysis provides an alternative point of view with respect to an earlier suggested assignment of the vibrational modes, which relates them to the stretching and bending vibrational modes of AlO_n ($n = 4, 5, \text{ and } 6$) polyhedra. Our assignment is based on the additive decomposition of the VDOS and $\epsilon_2(\omega)$ spectra, which shows that (i) the band at $\sim 380\text{ cm}^{-1}$ features oxygen motions occurring in a direction normal to the plane defined by the three nearest-neighbor aluminum atoms, i.e., *out-of-plane* motions of oxygen atoms; (ii) Al-O stretching vibrations (i.e., *in-plane* motions of oxygen atoms) appear at frequencies above $\sim 500\text{ cm}^{-1}$, which characterize the vibrational modes underlying the band at $\sim 630\text{ cm}^{-1}$. Aluminum and fourfold-coordinated oxygen atoms contribute uniformly to the VDOS and $\epsilon_2(\omega)$ spectra in the frequency region $\sim 350\text{--}650\text{ cm}^{-1}$ without causing specific features. Our numerical results are in good agreement with the previous and presently obtained experimental data on the IR dielectric function of am- Al_2O_3 films. Finally, we show that the IR spectrum can be modeled successfully by assuming isotropic Born charges for aluminum atoms and fourfold-coordinated oxygen atoms, while requiring the use of three parameters, defined in a local reference frame, for the anisotropic Born charges of threefold-coordinated oxygen atoms.

DOI: [10.1103/PhysRevMaterials.7.045604](https://doi.org/10.1103/PhysRevMaterials.7.045604)**I. INTRODUCTION**

Aluminum oxide (Al_2O_3) is a technologically relevant material used in a wide variety of applications [1–6]. In particular, polymorphs of Al_2O_3 possess chemical inertness,

thermal stability, and high dielectric properties [7]. In recent decades, the electronic properties of amorphous alumina (am- Al_2O_3) have made it an attractive dielectric-insulator material for use as a high- κ material [5] and for the development of supercapacitors [7,8]. Also, the nanocomposites based on the am- Al_2O_3 matrix have been explored for applications in harsh environments, for instance to produce fuel cladding for Generation IV systems [4,9], and as scratch-resistant coatings [10]. Finally, the heat transport properties of am- Al_2O_3 are

^{*}giacomazzi@iom.cnr.it[†]n.s.shcheblanov@gmail.com

also an active field of research [2,11], the understanding of which is ultimately associated with the correct description of the vibrational modes.

Al_2O_3 presents a variety of crystalline phases (e.g., α , γ , δ , η , θ , κ). This structural polymorphism reflects the predominant ionic nature of the Al-O bond, which entails a large variability in the O-Al-O bond angle and in local structures, which can be composed of both tetrahedral and octahedral Al units. Amorphous Al_2O_3 can be produced in different forms, e.g., anodic or evaporated films. The atomic structure of am- Al_2O_3 thin films has been the object of many experimental investigations in the past two decades. For instance, high-resolution solid-state NMR studies have shown that the fractions of fourfold- and fivefold-coordinated Al atoms (i.e., AlO_4 and AlO_5 units) are dominant in these films reaching ~ 92 – 95% [12–14]. A subsequent first-principles study [15] confirmed this fact for the densities of model structures of 2.9, 3.1, and 3.3 g/cm^3 . The fivefold coordination of Al atoms can be regarded as a fingerprint of the amorphous phase [16], which eventually might be relevant for catalysis applications [6]. Crystallization phenomena lead to the formation of edge-sharing sixfold-coordinated Al polyhedra (i.e. AlO_6 units) together with threefold- and fourfold-coordinated O atoms (i.e., OAl_3 and OAl_4 units) while the fivefold-coordinated Al atoms undergo annihilation [16,17]. Recent structural investigations (x-ray, neutron, and NMR) of amorphous and deeply supercooled liquid alumina were carried out by Shi *et al.* [18] and Hashimoto *et al.* [19], which also support the presence of high populations of AlO_4 and AlO_5 units predominantly linked by triply shared O atoms.

Unlike various glass-forming oxides (e.g., SiO_2 , GeO_2 , B_2O_3 , P_2O_5 , etc.), for am- Al_2O_3 , as far as we know, there are still no experimental data on inelastic scattering of neutrons or x-rays that provide a vibrational density of states (VDOS), with the exception of nanoparticle shells in the boson peak frequency range [20]. Infrared (IR) spectroscopy is the most widely used experimental technique to investigate vibrational properties in am- Al_2O_3 thin films [21–25], but despite this fact, the vibrational bands in the frequency range from ~ 300 to 700 cm^{-1} are still assigned in the literature to not so well specified AlO_4 , AlO_5 , and AlO_6 stretching vibrational modes [26]. Moreover, previous theoretical approaches ranging from *classical* and *ab initio* molecular dynamics (MD) [27–29] to neural network schemes [30] do not lead to a reliable analysis for the assignment of the vibrational modes.

To the best of our knowledge, experimentally derived complex dielectric functions, $\epsilon(\omega) = \epsilon_1(\omega) + i\epsilon_2(\omega)$, for high-quality am- Al_2O_3 films have been provided only in a few cases [21,31]. In particular, in Ref. [21] the dielectric function was derived from the experimental transmittance and reflectance data by using Fresnel's equations. However, there is a problem with these experimental data, in particular that these data extrapolate to a rather low static dielectric limit, $\epsilon_1(\omega \rightarrow 0) \sim 7$, compared to typical values obtained for beam-evaporated alumina films (~ 8 – 9) [32–35]. It should be noted that the technique used in Ref. [21] requires a nonreflecting substrate, high film homogeneity, low surface roughness, and sufficiently large thickness to ensure that no light returns from the inner sample to the sample surface. In addition, the quality of the experimental data depends on the

proper choice and treatment (subtraction) of the substrate as well as from the evaluation of the refraction index $n = \sqrt{\epsilon_\infty}$. All of these factors can be the cause of the aforementioned inconsistencies. As a result, all these contradictions, both experimental and theoretical, prompt us to undertake a new combined numerical-experimental study.

In this work, we primarily focus on the origin of the vibrational modes of am- Al_2O_3 giving rise to the experimental IR features peaking at ~ 380 and ~ 600 – 630 cm^{-1} in the $\epsilon_2(\omega)$ dielectric function. To elucidate the physics behind these features, we perform a complementary analysis based on high-quality experimental IR measurements (of am- Al_2O_3 thin films prepared by using an electron-beam evaporation), and first-principles calculations based on density functional theory (DFT). We provide detailed numerical modeling of the IR and VDOS spectra, and we reveal the contributions of the chemical species (O and Al) and various atomic units through additive decomposition approach. In particular, we point out the primary role of the motions of threefold-coordinated O atoms in directions normal and parallel to the plane of the neighboring Al atoms. Such a comprehensive analysis provides a solid ground for the assignment of the vibrational modes and specific IR features of am- Al_2O_3 . Based on the analysis of the calculated Born effective charges, we outline a parametric model that, despite its simplicity, reflects the underlying physics and allows us to calculate the dielectric function at a level comparable to *ab initio* quality.

This paper is organized as follows. In Sec. II we provide computational details of the DFT calculations (Sec. II A), and the physical properties of the am- Al_2O_3 models used for this study are discussed in Sec. II B. Experimental details concerning the synthesis, structural analysis, and IR spectra measurements are given in Sec. II C. In Sec. III A, we address structural properties such as coordination numbers and composition of the OAl_3 units for threefold-coordinated oxygen atoms, and we also analyze short- and medium-range orders using the Al-O bond-length and void distributions. Section III B is devoted to vibrational modes, and, in particular, we present an analysis of the VDOS spectra. In Sec. III C, we present results for the calculated and measured IR dielectric functions, and the static and high-frequency dielectric constants, while in Sec. III D we provide an analysis of the dynamical Born charges needed to define a parametric model for calculating IR spectra. Section IV is devoted to a discussion of the results. The conclusions of this work are drawn in Sec. V.

II. METHODS

A. *Ab initio* computational details

All the calculations for am- Al_2O_3 carried out in this work are based on DFT, using the generalized gradient approximation (GGA) [i.e., the Perdew-Burke-Ernzerhof (PBE) [36] functional] and norm-conserving pseudopotentials for O and Al atoms [37,38]. The Kohn-Sham wave functions are expanded in a basis of plane waves up to a kinetic energy cutoff of 70 Ry at the sole Γ -point of the Brillouin zone, as justified by the large size and the large band gap of the considered system [39].

The structural models of am- Al_2O_3 (Sec. II B) are relaxed by adopting a force threshold of $0.0025 \text{ eV}/\text{\AA}$, which allows

for a proper harmonic treatment of the vibrational modes. We calculate the vibrational frequencies and eigenmodes as well as the high-frequency dielectric constant and the dynamical Born charges within the linear-response approach [40]. In addition, the vibrational modes are obtained under the constraint that the force constants satisfy the *acoustic sum rule*. The codes used here for calculating structural and vibrational properties are freely available with the QUANTUM ESPRESSO package [40].

B. am-Al₂O₃ model structures

In our study, we use several structural models of am-Al₂O₃. The first structural model (hereafter named model I) was generated in Ref. [39] via Born-Oppenheimer MD simulations following a quench-from-the-melt approach. The initial configuration was obtained by adapting a 160-atom model of κ -Al₂O₃ to an orthorhombic supercell. The alumina melt was equilibrated at 3000 K for 1 ps and subsequently quenched to 300 K in 14 ps. The atomic structure was then further relaxed by constraining the shape of the supercell and by allowing the lattice constants to relax freely in order to remove the residual stress. The final model contains 160 atoms in a (periodic) orthorhombic simulation cell with sides: 11.475, 11.244, and 12.778 Å, corresponding to a density of 3.3 g/cm³. The *neutron* radial distribution function (RDF) calculated for this model [39] is found in fair agreement with experimental data from Ref. [41]. For the present work, we have just further relaxed the atomic configuration (generated in Ref. [39] and available in Ref. [42]) as explained in Sec. II A.

Two other models, hereafter named model II and model III, were generated in Ref. [27] (and named there as model G and model H, respectively). Models II and III both contain 120 atoms in an orthorhombic periodic supercell with a density of 3.27 and 3.22 g/cm³ [27], respectively. The models were generated by means of classical MD through a quench-from-the-melt procedure using the empirical pairwise potential developed by Matsui in Ref. [43], and then employed in DFT calculations within the local density approximation (LDA) to obtain the dielectric response [27,44]. Structure factors and RDFs of models II and III have been discussed in Ref. [27], and found to be consistent with other classical MD results and experiments. In the present work, the atomic configurations of these models have been only further relaxed by first-principles as explained in Sec. II A.

To analyze the medium-range-order structure of our am-Al₂O₃ models, we perform a void size distribution (VSD) analysis by using the Zeo++ code [45], an open source software that carries out a geometry-based analysis of porous materials and their voids (pores). In this analysis, every atom is considered as a sphere, and the radii of Al and O atoms are 1.23 and 0.73 Å, respectively [46]. A probe radius of 0.1 Å is used to scan empty space and find voids, i.e., spheres that can be inserted in contact with surrounding atoms without intersecting with them. Thus, the resulting VSD shows us how much void space corresponds to certain void sizes.

C. Experimental methods

Amorphous Al₂O₃ films are deposited on the surface of a 500- μ m-thick undoped Si single-crystal wafer by using an

electron-beam evaporation (Angstrom Engineering AMOD) with the substrate at room temperature and a base pressure of 5×10^{-5} Torr. The evaporation source is high-purity Al₂O₃ and the deposition rate is 1 Å/s and controlled by a quartz crystal microbalance. The nominal thickness is 300 nm for FTIR spectroscopy measurements and 100 nm for x-ray reflectivity (XRR) measurements. The high-resolution transmission electron microscopy (HR-TEM) imaging and x-ray diffraction are used to reveal the amorphous nature of the Al₂O₃ film. Applying the XRR technique gives a density of 2.74 g/cm³ and shows a low surface roughness of 1.1 nm. The reader is referred to Fig. S1 and related text in the Supplemental Material [47] for more information on film characterization.

IR spectra are recorded using Bruker Vertex 70V IR spectrometer in transmission mode under vacuum. A total of 64 scans are averaged with a resolution of 2 cm⁻¹. A blank Si wafer is used for background recording. The traces of atmospheric water and CO₂ were removed using atmospheric compensation in OPUS software (Bruker Optik GmbH). The spectra are smoothed by using the Savitzky-Golay algorithm and leveled to zero absorption at 4000 cm⁻¹. In addition to the broad absorption between ~ 100 and ~ 1100 cm⁻¹, there is a weak but broad absorption between ~ 3000 and ~ 3600 cm⁻¹. This band pattern can be assigned to the stretching vibrations of surface hydroxyl groups [48].

For calculating optical constants $n(\omega)$ and $k(\omega)$, related to the complex refractive index $\tilde{n}(\omega) = n(\omega) + ik(\omega)$, we follow the procedure developed by Gerakines and Hudson [49]. This iterative procedure requires as input a transmission spectrum with a reference refractive index of the film, its thickness, and optical constants for the substrate over the same wave-number range as the transmission spectrum. At each iteration, the Kramers-Kronig relation is used to obtain $n(\omega)$ from $k(\omega)$ for each wave number. The method is preferred in systems where obtaining a pure substance is challenging (e.g., in thin films), because it is hard to avoid multiple reflections and inferences when using reflective substrates.

III. RESULTS

A. Structural analysis

Before addressing the vibrational spectra of am-Al₂O₃ presented in the next subsections, we provide here some basic information about the structure of the am-Al₂O₃ models used in this study. In particular, in Table I we provide the coordination numbers of Al and O atoms, which is the most essential information for describing the local atomic arrangement (short-range order) in am-Al₂O₃. Model I features a large fraction ($\sim 70\%$) of fivefold- and sixfold-coordinated Al atoms with a smaller content of fourfold-coordinated Al atoms ($\sim 30\%$), in contrast to models II and III where the fraction of fourfold-coordinated Al atoms ($\sim 50\%$) is comparable to the total amount of fivefold- and sixfold-coordinated Al atoms. In model I, the vast majority (75%) of the O atoms are threefold-coordinated (to Al atoms), while the remaining 25% show fourfold coordination. The fractions of O atoms that are threefold-coordinated are even larger in models II and III, reaching up to 91.7%, although some of the O atoms in

TABLE I. Frequency (%) of coordination numbers of Al and O atoms in the am- Al_2O_3 models used in this study, obtained after *ab initio* relaxation in PBE [50]. Experimental coordination frequencies, obtained from the ^{27}Al MAS NMR spectra of Ref. [19] (anodized alumina) and Ref. [17] (PVD film), are also given. The cutoff radius of $R_{\text{cut}} \simeq 2.25 \text{ \AA}$ is used.

Coordination	Al			O		
	4	5	6	2	3	4
Model I	29.7	53.1	17.2		75.0	25.0
Model II	50.0	39.6	10.4	1.4	91.7	6.9
Model III	52.1	43.7	4.2	8.3	82.0	9.7
Expt. [19]	37.5	52.1	10.3			
Expt. [17]	48 ± 4	45 ± 4	7 ± 2			

these models are even found to be twofold-coordinated (1.4 and 8.3% in models II and III, respectively). Models II and III show Al coordination numbers in reasonable agreement with the experimental estimate of Refs. [13,17,19], with minor differences with respect to the LDA-DFT results of Ref. [27], of which the most noticeable one concerns the low number of fivefold-coordinated Al atoms, which has been found to increase by 10% upon the generation of model II [27]. On the other hand, model I shows a larger average Al coordination due to the larger number of sixfold- and fivefold-coordinated Al atoms. Incidentally, we note that, in spin-coated am- Al_2O_3 films, large fractions ($\sim 20\%$) of sixfold-coordinated Al atoms have been estimated by using NMR spectroscopy [51]. Indeed, the structure of am- Al_2O_3 films depends on the method of synthesis and on the deposition conditions [17,51,52], which can lead to structural changes, typically corresponding to fluctuations up to $\sim 10\%$ of the coordination frequencies of Al (see Table I). In particular, am- Al_2O_3 resulting from solution processing such as sol-gel and spin-coating can exhibit large fractions of sixfold-coordinated Al atoms due to the presence of hydroxyl groups, residual hydrogen, or hydration [17].

The NMR investigation of Ref. [17] provided evidence that threefold-coordinated O atoms in am- Al_2O_3 can be distinguished from threefold-coordinated O atoms in transition alumina phases, like θ - and γ -alumina. In fact, the threefold-coordinated O atoms in the crystal structure are found to form a particular structural motif with one fourfold- and two sixfold-coordinated Al atoms (i.e., $\text{O}^{[4]\text{Al}^{[6]\text{Al}}_2]$). By contrast, Ref. [17] suggests that in am- Al_2O_3 the dominant configurations are $\text{O}^{[4]\text{Al}^{[5]\text{Al}}]$ and $\text{O}^{[4]\text{Al}^{[5]\text{Al}}_2]$, while the occurrence

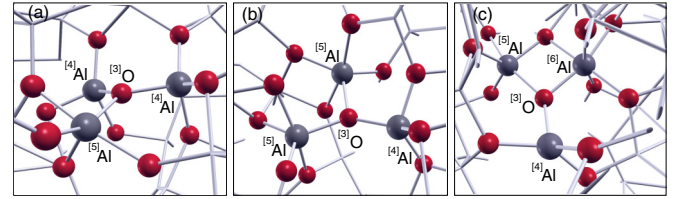


FIG. 1. Ball and stick models [53] of the dominant OAl_3 units as found in the investigated am- Al_2O_3 models: (a) an $\text{O}^{[4]\text{Al}^{[5]\text{Al}}]$ unit, (b) an $\text{O}^{[4]\text{Al}^{[5]\text{Al}}\text{Al}^{[6]\text{Al}}]$ unit, and (c) an $\text{O}^{[4]\text{Al}^{[5]\text{Al}}\text{Al}^{[6]\text{Al}}]$ unit. Oxygen atoms (red balls) and aluminum atoms (gray balls) are shown. For clarity, only atoms belonging to the OAl_3 unit are displayed.

of configurations featuring only sixfold-coordinated Al atoms, such as $\text{O}^{[6]\text{Al}}_3$, should be negligible.

In Table II we give the results of the analysis of OAl_3 units in our models, and in particular we confirm that the dominant configurations (Fig. 1) in am- Al_2O_3 models are $\text{O}^{[4]\text{Al}^{[5]\text{Al}}]$ and $\text{O}^{[4]\text{Al}^{[5]\text{Al}}_2]$ as they sum up to $\sim 50\%$ of the OAl_3 units ($\sim 56\%$ in model III). Yet, we also find an important fraction of $\text{O}^{[4]\text{Al}^{[5]\text{Al}}\text{Al}^{[6]\text{Al}}]$ units, which have to be considered as typical of the amorphous phase because of the occurrence of a fivefold-coordinated Al atom, and which could be relevant in the context of crystallization [17]. The low concentration of $\text{O}^{[4]\text{Al}^{[6]\text{Al}}_2]$ in our models indicates a marked structural difference with respect to θ - or γ -alumina crystalline phases, and it is consistent with the amorphous nature of our model structures [17].

The threefold-coordinated O atoms are found to approximately lie on the plane of their three Al neighbors. To evaluate the planarity of these units, we define the ratio π_d as obtained by dividing the sum over the three Al-O-Al angles by 360° , which at most equals 1 for an ideal planar unit. About 80% of OAl_3 units in our models show a quite high degree of planarity, with a π_d larger than 0.95 (i.e., with a sum of angles of 342°), comparable to the degree of planarity of OAl_3 units in θ -alumina. In particular, we find that $\text{O}^{[4]\text{Al}}_3$ and $\text{O}^{[4]\text{Al}^{[5]\text{Al}}]$ are highly planar with an average π_d of 0.987 and 0.978, respectively.

The mean Al-O bond lengths for models I, II, and III are 1.88, 1.85, and 1.84 \AA , respectively. The average Al-O bond lengths for models II and III are in rather good agreement with the peak of the experimental neutron RDF of Ref. [19] located at 1.81 \AA . Compared to the LDA-DFT simulation [27], we register a slight increase (by $\sim 0.10 \text{ \AA}$) of the mean Al-O bond length for models II and III. Moreover, the calculated average Al-O bond-lengths of the AlO_4 , AlO_5 , and AlO_6 polyhedra in our models are 1.79, 1.89, and 1.96 \AA , respectively. Hence, the

TABLE II. Composition (%) of OAl_3 units by the coordination number of neighboring Al atoms of the central threefold-coordinated O atom. Minor fractions related to OAl_3 units with only highly coordinated Al atoms (i.e., $\text{O}^{[6]\text{Al}}_3$) are omitted for clarity. For each type of OAl_3 units, the average degree of planarity π_d is indicated. The cutoff radius of $R_{\text{cut}} \simeq 2.25 \text{ \AA}$ is used.

	$^{[4]\text{Al}}_3$	$^{[4]\text{Al}^{[5]\text{Al}}]$	$^{[4]\text{Al}^{[5]\text{Al}}_2]$	$^{[4]\text{Al}^{[6]\text{Al}}]$	$^{[4]\text{Al}^{[6]\text{Al}}_2]$	$^{[4]\text{Al}^{[5]\text{Al}}\text{Al}^{[6]\text{Al}}]$	$^{[5]\text{Al}}_3$
Model I	2.8	11.1	36.1	4.2	4.2	15.3	11.3
Model II	9.1	18.2	22.7	15.2	3.0	22.7	3.0
Model III	8.5	30.5	25.4	8.5	1.7	11.9	11.9
π_d	0.987	0.978	0.961	0.972	0.957	0.969	0.972

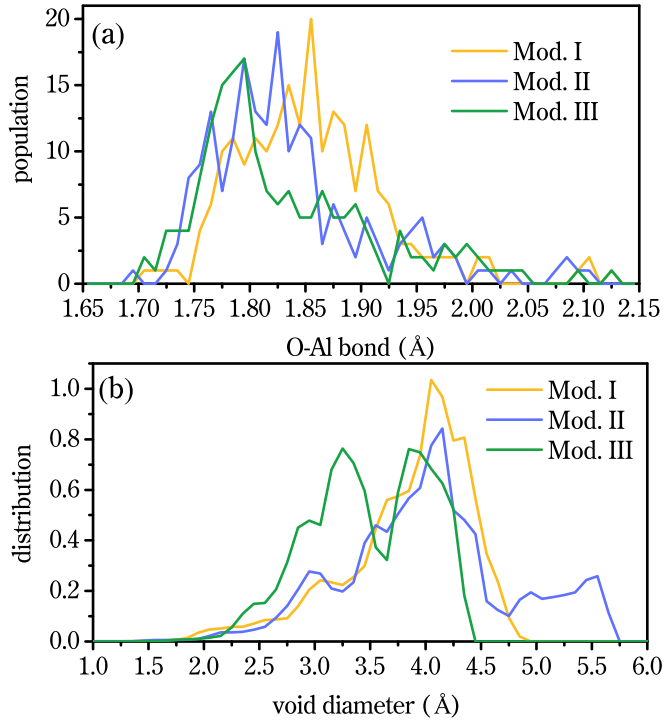


FIG. 2. (a) Distribution of O-Al bond lengths for threefold-coordinated oxygen atoms for models I, II, and III. (b) Void size distribution for the same models.

slightly longer mean Al-O bond length of model I reflects the higher number of AlO_6 polyhedra and the smaller number of AlO_4 tetrahedra in this model as compared to models II and III (see Table I). On the other hand, the calculated average O-Al bond lengths in our models for twofold-, threefold-, and fourfold-coordinated O atoms are 1.72, 1.85, and 1.95 Å, respectively, with some minor variations among models (~ 0.01 Å) and with a rather large spread of about 0.04 Å in the bond distributions.

In Figs. 2(a) and 2(b) we provide the distribution of O-Al bond lengths for threefold-coordinated O atoms and the void distribution analysis for the three alumina models. The Al-O bond-length distributions of models II and III show peaks at ~ 1.82 and ~ 1.78 Å, respectively. The Al-O bond distribution of model I shows a shift towards longer bonds, as indicated by its peak located at ~ 1.86 Å with respect to the distributions of models II and III. This value overestimates by 0.05 Å the experimental bond length [19]. This is also consistent with the differences between the mean Al-O bond lengths in our models, indicating that threefold-coordinated O are still rather well representing the O-Al bond distribution.

The density of alumina films may vary due to its porosity and this can affect the dielectric function [31]. Although a discussion of porosity in alumina is beyond the scope of the present paper, it is of some interest to evaluate the distribution of voids in our models. This will also give a measure of the “openness” of the alumina network structure. Despite the fact that all the models have similar material densities, although slightly smaller in model III than in model I, we note that the VSD shown in Fig. 2(b) is substantially different in the three models. Moreover, from the positions of the main peaks of

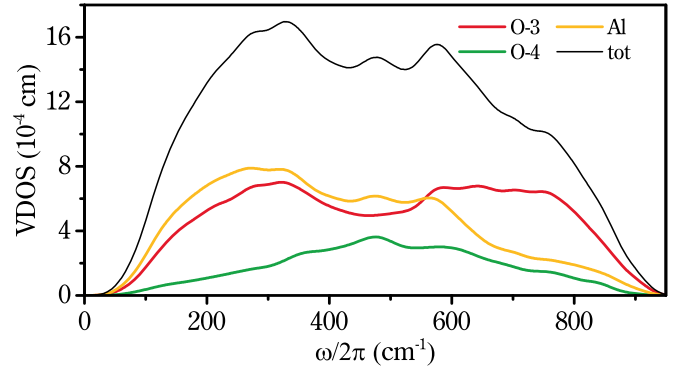


FIG. 3. Total VDOS (solid black) with its decomposition, as defined by Eq. (2), in terms of the contribution of aluminum (solid yellow), threefold-coordinated (solid red), and fourfold-coordinated (solid green) oxygen atoms. Analysis made for the model I of Ref. [39]. A Gaussian broadening of 20 cm^{-1} is used.

the VSDs in Fig. 2(b), one is brought to assume that a greater porosity corresponds to longer bonds, i.e., that the population of bond lengths correlates with the VSD.

B. Vibrational density of states

The vibrational density of states $\rho(\omega)$ is calculated as

$$\rho(\omega) = \frac{1}{3N} \sum_n \delta(\omega - \omega_n), \quad (1)$$

where N is the total number of atoms in the model and ω_n is the vibrational frequency of the n th vibrational eigenmode ξ_I^n . In addition, we consider the atomic contributions of the Al and differently coordinated O subpopulations:

$$\rho_\alpha(\omega) = \frac{1}{3N} \sum_n \sum_{I \in \alpha} |\xi_I^n|^2 \delta(\omega - \omega_n), \quad (2)$$

where $\alpha = \text{Al}$ or O and the index I enumerates the atoms.

In Fig. 3, we show the total VDOS for model I of the am- Al_2O_3 along with its decomposition in terms of oxygen and aluminum contributions as defined in Eq. (2). The calculated VDOS spectrum extends up to $\sim 950 \text{ cm}^{-1}$. Several bands can be discerned and interpreted thanks to the atomic decomposition. The two bands peaked at ~ 320 and $\sim 590 \text{ cm}^{-1}$ reflect underlying features related to threefold-coordinated O atoms. The central band peaking at $\sim 470 \text{ cm}^{-1}$ corresponds to the contribution of fourfold-coordinated O atoms to the total VDOS. The localization of vibrational modes is studied by using the mode participation ratio [54,55], which is shown in Fig. S2 in the Supplemental Material [47]. It can be noted that the modes between 200 and 400 cm^{-1} are not spatially localized on individual OAl_3 units, while the stretching modes above 500 cm^{-1} show a tendency to become much more spatially localized.

In Fig. 4, we consider threefold-coordinated O atoms, and we demonstrate that there is a correlation between the O-Al bond lengths associated with these O atoms and the O-Al stretching frequencies ω_{max} . These frequencies are calculated by first finding the projections $\mathcal{P}_{\text{OAl}}(\omega)$ of the oxygen displacements, ξ_I^n , onto the O-Al directions for each one of

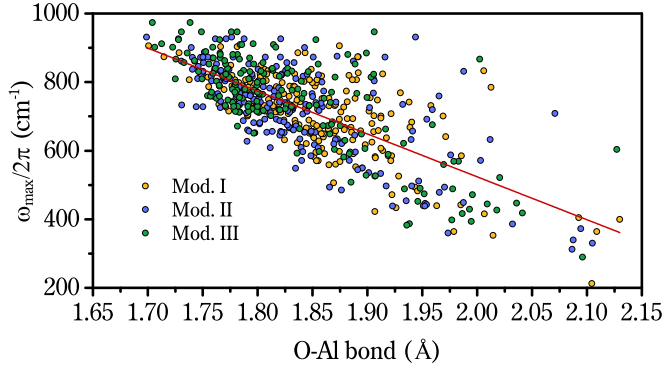


FIG. 4. Stretching frequency vs O-Al bond length for models I (yellow disks), II (blue disks), and III (green disks) (see text for more details). The solid (red) line corresponds to a linear fit of all the data.

the three neighboring Al atoms, and then by looking at the frequency position of the peak of $\mathcal{P}_{\text{OAl}}(\omega)$. The linear interpolation obtained by fitting the stretching frequencies ω_{max} for all threefold-coordinated O atoms of the three models under study shows that the O-Al stretching frequency ω_{max} decreases with increasing bond lengths with a slope of $\approx 1250 \text{ cm}^{-1}/\text{\AA}$. Since Al atoms with increasing oxygen coordination show longer Al-O bond-lengths (Sec. III A), this correlation allows us to explain the redshifts of the stretching bands in the spectra of our models as discussed in Sec. III C.

C. Infrared dielectric function

The real and imaginary parts of the dielectric response function, $\epsilon_1(\omega)$ and $\epsilon_2(\omega)$, are calculated here with the following expressions [56,57]:

$$\epsilon_1(\omega) = \epsilon_\infty - \frac{4\pi}{3\Omega} \sum_n \frac{|\mathcal{F}^n|^2}{\omega^2 - \omega_n^2}, \quad (3)$$

$$\epsilon_2(\omega) = \frac{4\pi^2}{3\Omega} \sum_n \frac{|\mathcal{F}^n|^2}{2\omega_n} \delta(\omega - \omega_n), \quad (4)$$

where Ω is the volume of the periodic simulation cell, and $\epsilon_\infty = \frac{1}{3}\text{Tr}(\epsilon_\infty)$ is the high-frequency (electronic) dielectric constant. The oscillator strengths \mathcal{F}^n can be calculated from the Born charges Z_I^* and eigenmodes ξ_I^n as

$$\mathcal{F}_j^n = \sum_I \mathcal{F}_{Ij}^n = \sum_I \sum_k Z_{I,jk}^* \frac{\xi_{Ik}^n}{\sqrt{m_I}}, \quad (5)$$

where m_I is the atomic mass of the atom I . We also introduce a coupling function as follows:

$$C_{\text{IR}}(\omega) = \epsilon_2(\omega)/\rho(\omega), \quad (6)$$

where $\rho(\omega)$ is the VDOS given by Eq. (1).

Similar to the Raman additive decomposition (see Refs. [55,58]), the IR spectrum can be recast as

$$\epsilon_2(\omega) = \frac{4\pi^2}{3\Omega} \sum_n \sum_\alpha \frac{\{\mathcal{F}^n\}_\alpha^2}{2\omega_n} \delta(\omega - \omega_n), \quad (7)$$

where

$$|\mathcal{F}^n|^2 = \sum_\alpha \{\mathcal{F}^n\}_\alpha^2 = \sum_\alpha \left\{ \sum_{\alpha'} (\mathcal{F}_\alpha^n \cdot \mathcal{F}_{\alpha'}^n) \right\}, \quad (8)$$

TABLE III. Density, ρ (g/cm^3), static dielectric constant, ϵ_0 , high-frequency dielectric constant, ϵ_∞ , and lattice contribution, ϵ_{lat} , as calculated for models I, II, and III of am- Al_2O_3 in this work. The experimental data are presented for am- Al_2O_3 films obtained by various methods. Data for ρ are taken from Refs. [31,60,61], those for ϵ_0 from Refs. [32,33,62], and those for ϵ_∞ from Refs. [34,35,63].

	ρ	ϵ_0	ϵ_{lat}	ϵ_∞
Model I	3.30	11.44	8.26	3.18
Model II	3.27	10.33	7.21	3.12
Model III	3.22	11.11	8.01	3.10
Expt.	2.5–3.4	8–11		2.5–2.9
Expt. (present)	2.74	~ 9		~ 2.72

with the α th oscillator strengths given by

$$\mathcal{F}_\alpha^n = \mathcal{F}_{\alpha j}^n = \sum_{I \in \alpha} \mathcal{F}_{Ij}^n. \quad (9)$$

We evaluate the static dielectric constant ϵ_0 , which can be written in terms of the electronic ϵ_∞ and lattice ϵ_{lat} contributions [57] as

$$\epsilon_0 = \epsilon_\infty + \epsilon_{\text{lat}}, \quad (10)$$

$$\epsilon_{\text{lat}} = \frac{4\pi}{3\Omega} \sum_n \frac{|\mathcal{F}^n|^2}{\omega_n^2}. \quad (11)$$

The dielectric function described above gives access to all the dielectric properties. In particular, to access longitudinal optical modes, we hereafter address the so-called energy loss function, which can be written in terms of the complex dielectric function $\epsilon(\omega)$, by using directly Eqs. (3) and (4):

$$-\text{Im} \left[\frac{1}{\epsilon(\omega)} \right] = \frac{\epsilon_2(\omega)}{\epsilon_1^2(\omega) + \epsilon_2^2(\omega)}. \quad (12)$$

However, the loss function can also be obtained through a direct calculation [56,59] by using the longitudinal modes as follows:

$$-\text{Im} \left[\frac{1}{\epsilon(\omega)} \right] = \frac{4\pi^2}{\Omega(\epsilon_\infty)^2} \sum_n \frac{(\hat{\mathbf{q}} \cdot \mathcal{F}^n)^2}{2\omega_n} \delta(\omega - \omega_n), \quad (13)$$

where \mathcal{F}^n is calculated by using ω_n and ξ_I^n obtained by diagonalizing the full dynamical matrix $\mathcal{D}_{Ii,Jj}^{\mathbf{q} \rightarrow 0}$ [59]. For isotropic systems, the energy loss function in Eq. (13) can be averaged over all directions $\hat{\mathbf{q}}$. Here, we use the three Cartesian directions for this average. In Table III, we give the static dielectric constants calculated for models I, II, and III, together with the high-frequency dielectric constants and the lattice contributions, in comparison with experimental data. The values of the static dielectric constant given in the literature depend on the method of preparation, e.g., ϵ_0 is 8.3 for electron-beam evaporated films [32–34], while Ref. [64] gives values ranging from 9.8 to 13.3 for barrier-type aluminum oxides. For films obtained by atomic layer deposition (ALD), one finds in Ref. [62] a value of 11, while Kübler [32] provides ≈ 9.0 below 10 Hz at room temperature for films prepared by ion-assisted evaporation. The densities of am- Al_2O_3 films also vary significantly depending on the production method, e.g., densities of ~ 3.1 – $3.4 \text{ g}/\text{cm}^3$ have been reported for

magnetron-sputtered alumina films [60,61], while a value of 2.45 g/cm^3 has been measured for sol-gel prepared alumina films [31]. Beam-evaporated alumina films, such as those investigated in this study, typically show a density range of $\sim 2.6\text{--}3.1 \text{ g/cm}^3$ [32,65]. The experimental values of the high-frequency electronic dielectric constant ϵ_∞ of am- Al_2O_3 films range from 2.5 to 2.9, which corresponds to a high-frequency refractive index n between ~ 1.6 and ~ 1.7 (at wavelengths around $1 \mu\text{m}$) [34,35,61,63], with slight variations depending on the preparation method.

The calculated density of the studied am- Al_2O_3 models is about $3.2\text{--}3.3 \text{ g/cm}^3$ and lies in the range of experimentally recorded densities (Table III). The electronic dielectric constant ϵ_∞ shows only minor variations between models ($\sim 3\%$), which have slightly different densities (see Table III). Also, the PBE-DFT results for models II and III show only minor differences ($\lesssim 1.5\%$) compared to the LDA-DFT results [44]. In contrast, the lattice contribution ϵ_{lat} is quite sensitive to the details of the VDOS, as indicated by the rather large differences between the models in Table III (see also Ref. [27]). Compared to the LDA-DFT results of Ref. [27], we have an increase of about 20% for the ϵ_{lat} in model III, while for model II we register a decrease of $\sim 2\%$, likely due to the fact that our VDOS does not show the strong peaks in the frequency range $50\text{--}100 \text{ cm}^{-1}$ found for the corresponding model G [27,44]. In Ref. [64], by using finite electric fields, a value of 3.03 was found for the high-frequency permittivity ϵ_∞ of model I, which only slightly underestimates the linear-response result in Table III. This is consistent with the results obtained with different methods for models containing about 100 atoms [66].

In Figs. 5(a) and 5(b), the dielectric functions $\epsilon_1(\omega)$ and $\epsilon_2(\omega)$ calculated for the three am- Al_2O_3 models are compared with the experimental ones obtained from the data on the transmittance and reflectance by using the Fresnel equations [21], and those measured in this work. While the experimental $\epsilon_1(\omega)$ of Refs. [21,67] gives a static limit of ~ 7 , the data measured in this work entail a larger value ~ 9 . The shapes of the $\epsilon_1(\omega)$ spectra shown in Fig. 5(a) are similar for both sets of experimental data, with a rather smooth step at $\sim 360\text{--}380 \text{ cm}^{-1}$ and a very broad minimum at $\sim 800 \text{ cm}^{-1}$. The dielectric function $\epsilon_1(\omega)$ calculated for all three models is rather noisy due to the finite-size effect, which limits the number of vibrational modes at low frequencies. For all the models, the static limit ($\sim 10\text{--}11$) is considerably larger than the experimental ones, because of (i) the slightly larger density, which may account for an increase of ϵ_∞ by ~ 0.4 (Table III), and (ii) the finite size of our models, which leads to vibrational modes being less accessible at low frequencies ($\lesssim 50 \text{ cm}^{-1}$, i.e., boson peak region). Despite these limitations, the shape of the $\epsilon_1(\omega)$ spectrum obtained by averaging over the three models agrees reasonably well with the experimental data.

The experimental $\epsilon_2(\omega)$ spectrum reported in Refs. [21,67] shows a very broad peak with a maximum at $\sim 630 \text{ cm}^{-1}$ together with an additional feature at $\sim 380 \text{ cm}^{-1}$. The experimental data obtained in this work present similar broad bands: the main band forming a *plateau* from ~ 570 to 620 cm^{-1} , peaking at $\sim 585 \text{ cm}^{-1}$, and the additional band showing a peak at $\sim 370 \text{ cm}^{-1}$. The intensity of both bands turns out to be

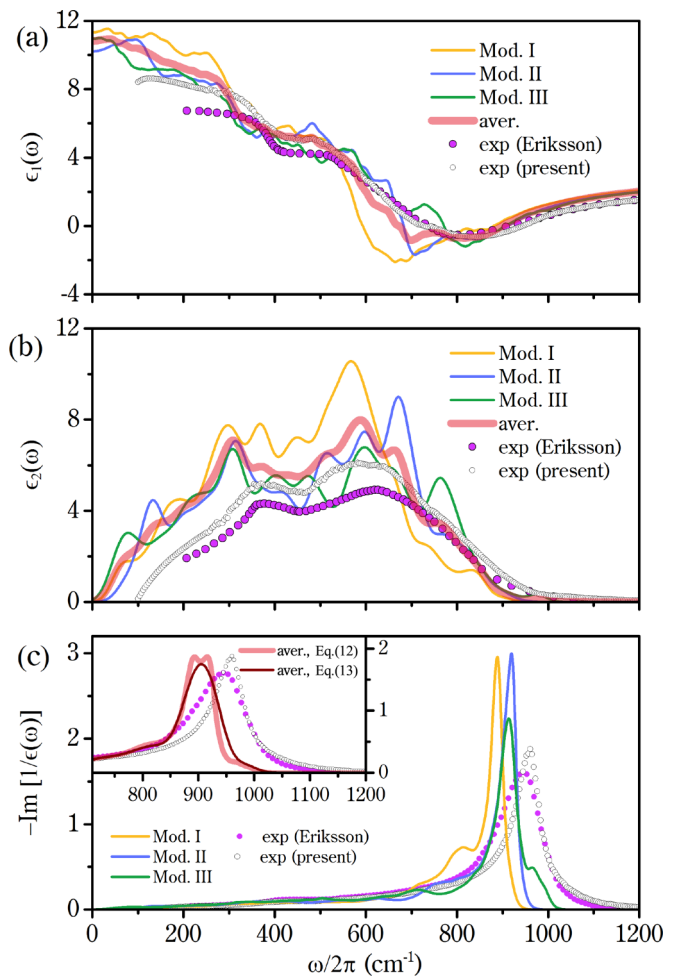


FIG. 5. (a) The real part of the dielectric function, $\epsilon_1(\omega)$, for model I (yellow curve), model II (blue curve), model III (green curve), and averaged over the three models (red). Experimental data from [21,67,68] (violet circles) and this work (black empty circles). (b) The same notations as in (a) but for the imaginary part, $\epsilon_2(\omega)$. (c) The same notations as in (a) but for the energy loss function, $-\text{Im}[1/\epsilon(\omega)]$, calculated by using Eq. (12). The inset in panel (c) shows a zoom of the loss function averaged over the three models calculated by using Eq. (12) (red curve) and Eq. (13) (brown curve). A Gaussian broadening of 20 cm^{-1} is used in all calculations.

significantly increased compared to previous measurements [21]. The main features of the $\epsilon_2(\omega)$ spectrum calculated for model I comprise a double peak at 305 and 370 cm^{-1} and a principal band peaked at $\sim 570 \text{ cm}^{-1}$, which exhibits a redshift with respect to the experimental data displayed in Fig. 5(b). The average Al-O bond length in model I is larger than in models II and III by about 0.03 \AA . Because of the trend shown in Fig. 4, this produces a redshift in the stretching region ($500\text{--}900 \text{ cm}^{-1}$) of the $\epsilon_2(\omega)$ spectrum of model I, compared to the spectra of the other two models. The spectra of models II and III show the first band at $\sim 320 \text{ cm}^{-1}$ and the second band extending from ~ 500 to $\sim 700 \text{ cm}^{-1}$, the main peaks of which are located at ~ 600 and 670 cm^{-1} in models III and II, respectively. The dielectric response for models II and III should be compared with the LDA-DFT results of Ref. [44], since our GGA-PBE models II and III are obtained by relaxation

of the LDA-DFT models (see details in Sec. II B). For model III, the results are very close to those reported in Ref. [44]. By contrast, for model II, our results do not show either any strong peak below $\sim 100 \text{ cm}^{-1}$, as was found in Ref. [44], or any important feature at $\sim 480 \text{ cm}^{-1}$. We attribute these differences to minor structural changes that occur upon the structural relaxation described in Sec. III A and to the different DFT setups. In addition, we note that porous am- Al_2O_3 can exhibit features in the $\epsilon_2(\omega)$ spectrum at low frequency, i.e., $\sim 100 \text{ cm}^{-1}$, but these do not occur in high-quality films of am- Al_2O_3 [31]. Overall, averaging over the three models gives an $\epsilon_2(\omega)$ spectrum in good agreement with the experimental one, except for a slight underestimation of the frequencies of the main peaks (by $\sim 10\%$) and an overestimation of the band intensities, which is typical for amorphous models of such size [69].

In Fig. 5(c), we show the loss function, $-\text{Im}[1/\epsilon(\omega)]$, calculated through Eq. (12). The transverse and longitudinal modes are revealed by the frequency position of the maxima in $\epsilon_2(\omega)$ and $-\text{Im}[1/\epsilon(\omega)]$ spectra, respectively [70]. A dominant high-frequency peak of $-\text{Im}[1/\epsilon(\omega)]$ at $\sim 900 \text{ cm}^{-1}$ is clearly visible for all models. In models II and III, the peaks occur at very close frequencies (920 and 915 cm^{-1}), while model I exhibits a peak at a slightly redshifted frequency 890 cm^{-1} , as a likely consequence of the trend explained above for the $\epsilon_2(\omega)$ spectrum. The peaks obtained by averaging the spectra [calculated by Eqs. (12) and (13)] over all models [see the inset in panel (c)], are located at $\sim 900 \text{ cm}^{-1}$, which is in good agreement (within $\sim 7\%$) with our experimental position of the high-frequency peak at $\sim 970 \text{ cm}^{-1}$ obtained by using Eq. (12). Moreover both the experimental data obtained in this work and in Ref. [21] produce peaks at close frequencies at about $950\text{--}970 \text{ cm}^{-1}$.

In the remainder of this subsection, in order to discuss the origin of the IR vibrational bands, we provide an atomic decomposition of the IR spectrum by using Eqs. (6) and (7). Next, we analyze the two main components underlying the IR spectrum: (i) the IR coupling functions given by Eq. (6); (ii) the squared displacement spectra in terms of relative weights of partial VDOSs given by Eq. (2). In Fig. 6(a), we show such a decomposition focusing on the imaginary part of the dielectric function, $\epsilon_2(\omega)$, of model III, the results for the other two models being similar. It can be seen that the main features come from contributions of *in-plane* and *out-of-plane* (perpendicular) motions of threefold-coordinated O atoms, the plane being defined by the three nearest-neighbor Al atoms. The vibrations related to the *out-of-plane* motion of these O atoms occur in the range $\lesssim 500 \text{ cm}^{-1}$ (dash blue), and they give a maximal contribution to $\epsilon_2(\omega)$ around $\sim 320 \text{ cm}^{-1}$. Vibrational modes featuring *in-plane* motions of threefold-coordinated oxygens cover the range $\gtrsim 400 \text{ cm}^{-1}$ (dash red) and become dominant above $\sim 500 \text{ cm}^{-1}$. The distinct separation of these contributions is due to different force constants associated with motions of threefold-coordinated O atoms in parallel (*stiff*) and perpendicular (*soft*) directions. Al atoms, being highly coordinated, do not possess prominent features and contribute to the $\epsilon_2(\omega)$ spectrum rather uniformly over the entire frequency domain ($\sim 50\%$). Twofold-coordinated O atoms provide a small contribution for frequencies below 400 cm^{-1} , and also at about 800 cm^{-1} (O-Al stretching mo-

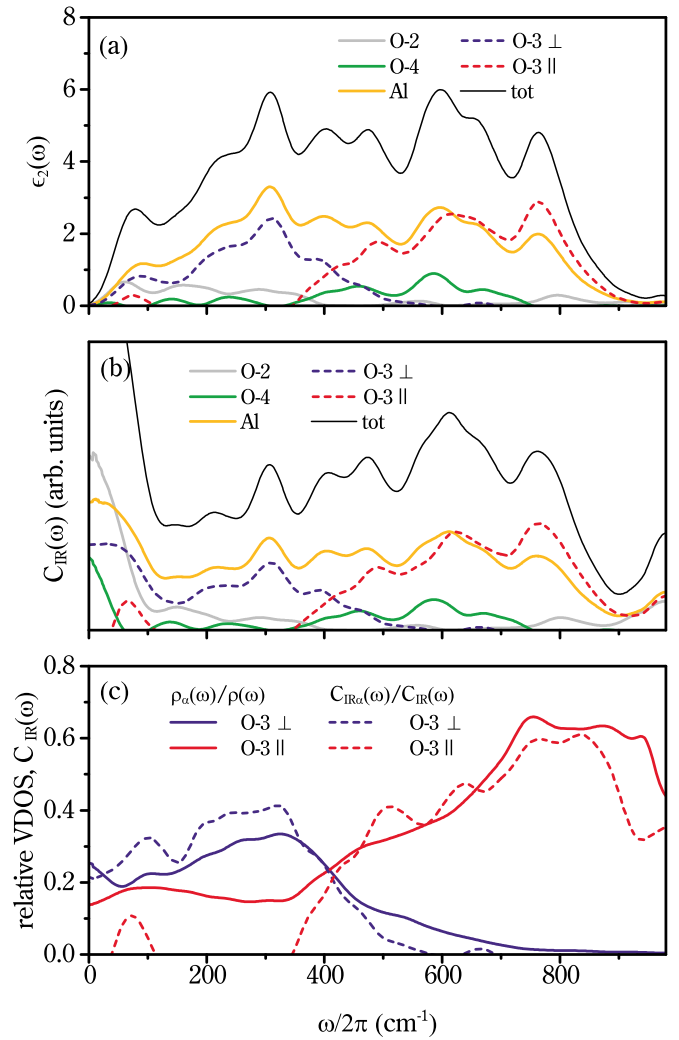


FIG. 6. Results for model III. (a) Decomposition of $\epsilon_2(\omega)$ into contributions from Al atoms (yellow) and from twofold-coordinated (solid light gray), fourfold-coordinated (solid green), and threefold-coordinated O atoms. Contribution of the latter is split into *out-of-plane*, i.e., perpendicular (dashed, blue) and *in-plane*, i.e., parallel (dashed, red) motions. (b) Decomposition of the IR coupling function $C_{\text{IR}}(\omega)$ with the same notations as in panel (a). (c) Comparison between the contributions of *out-of-plane* (blue) and *in-plane* (red) motions of threefold-coordinated O atoms in terms of the relative VDOS (solid) and relative IR coupling function (dashed) spectra.

tions). Fourfold-coordinated O atoms also give a rather minor contribution to the $\epsilon_2(\omega)$ spectrum in the frequency range going from 400 to 700 cm^{-1} . Thus, twofold- and fourfold-coordinated O atoms do not produce specific features in the $\epsilon_2(\omega)$ spectrum, because of their rare occurrence in all our am- Al_2O_3 models (as compared to threefold-coordinated O atoms, see Table I) and also because of the wide O-Al bond distribution associated with fourfold-coordinated O atoms, as indicated by its large spread of 0.04 \AA .

The atomic decomposition of the coupling function, $C_{\text{IR}}(\omega)$, given by Eq. (6), presented in Fig. 6(b), shows that the amplitude relations for the contributions of twofold-, threefold-, and fourfold-coordinated O atoms are quite similar

to the ones displayed by the $\epsilon_{2\alpha}(\omega)$ in Fig. 6(a), consistent with the fact that the VDOS is rather constant, without showing prominent peaks in the range from ~ 300 to 800 cm^{-1} . In Fig. 6(c) we show the relative partial VDOSs (or squared displacement spectra) $|\xi_{\alpha}(\omega)|^2 = \rho_{\alpha}(\omega)/\rho(\omega)$ that highlights the frequency ranges of *in-plane* and *out-of-plane* motions of threefold-coordinated O atoms. We also display the relative coupling functions [i.e., $C_{\text{IR}\alpha}(\omega)/C_{\text{IR}}(\omega) = \epsilon_{2\alpha}(\omega)/\epsilon_2(\omega)$], which present a substantial similarity to the relative partial VDOSs. The good agreement between the curves highlights (i) the dominant role of the *pure in-plane* and the *pure out-of-plane* vibrations, i.e., the interference effect, given by Eq. (8), is marginal, and (ii) the minor influence of the anisotropy and the orientation of the Born effective charge tensors. Thus, the functional dependence of the IR spectrum $\epsilon_2(\omega)$ on frequency is mainly determined by the weighted squared displacement spectra $\bar{Z}_{\alpha}^{-2} |\xi_{\alpha}(\omega)|^2$ and VDOS $\rho(\omega)$, i.e., $\epsilon_2(\omega) = \rho(\omega) \sum_{\alpha} C_{\text{IR}\alpha}(\omega) \sim \rho(\omega) \sum_{\alpha} \bar{Z}_{\alpha}^{-2} |\xi_{\alpha}(\omega)|^2$. Equivalently, we can recast $\epsilon_2(\omega)$ as a superposition of weighted partial VDOS spectra, i.e., $\epsilon_2(\omega) \sim \sum_{\alpha} \bar{Z}_{\alpha}^{-2} \rho_{\alpha}(\omega)$, where \bar{Z}_{α}^{-2} are average Born effective charges corresponding to α species, and where the O contribution can be further decomposed into *in-plane* and *out-of-plane* contributions. The next subsection is devoted to a detailed discussion of the Born effective charges.

D. Born charge tensors and parametric model

We analyze here the Born charges and discuss a parametric model that allows for the straightforward calculation of IR spectra provided that the atomic configuration, the vibrational modes, and their frequencies are available.

The overwhelming majority of O atoms in am- Al_2O_3 are threefold-coordinated with Al atoms (see Table I), while the O atom lies in the plane of its Al neighbors (see Sec. III A). Then, to analyze their Born charge tensors Z^* , it is convenient to introduce the following local reference frame: the first basis vector is chosen along the bisector of an Al-Al-Al angle (x direction) of the triangle with the Al neighbors at the vertices; the second basis vector is taken along the direction perpendicular to the plane defined by the three nearest-neighbor Al atoms (y direction); the last one can be found by the cross product of the first two basis vectors (z direction). Thus, OAl_3 units have an approximate *trigonal symmetry* (C_{3v}), with the symmetry axis lying in the y direction, according to our definition above. In this local reference system, we calculate \bar{Z}^* for the threefold-coordinated O atom (hereafter $^{[3]}O$) as an average over the three possible choices of the basis and over the three models:

$$\bar{Z}_{^{[3]}O}^* = \begin{pmatrix} -2.11 & 0.00 & 0.01 \\ 0.00 & -1.46 & 0.00 \\ 0.00 & -0.01 & -2.07 \end{pmatrix}. \quad (14)$$

The average isotropic charge, i.e., $Z_{\text{iso}}^* = \frac{1}{3} \text{Tr}(\bar{Z}^*)$, is found to be ≈ -1.89 . For each $^{[3]}O$ atom, we perform a decomposition of its Born charge tensor in terms of the representations of the spatial rotations [71]:

$$Z_{^{[3]}O}^* = Z_{\ell=0}^* + Z_{\ell=1}^* + Z_{\ell=2}^*, \quad (15)$$

TABLE IV. Average isotropic Born charges $\frac{1}{3} \text{Tr}(\bar{Z}^*)$ for Al atoms (\bar{Z}_{Al}^*) with four-, five-, and sixfold coordination and for O atoms (\bar{Z}_{O}^*) with two-, three-, and fourfold coordination. The given values correspond to the average values over atoms of all three models. The Born charges of $^{[3]}O$ atoms are described by the matrix given by Eq. (20). Standard deviations are given in parentheses.

Al	4	5	6
\bar{Z}_{Al}^*	2.73(0.1)	2.84(0.08)	2.93(0.07)
O	2	3	4
\bar{Z}_{O}^*	-1.82(0.03)	-1.89(0.05)	-1.95(0.03)

where the first term $Z_{\ell=0}^*$ is the isotropic term,

$$Z_{\ell=0}^* = Z_{\text{iso}}^* \delta_{ij}, \quad (16)$$

and the two traceless terms $Z_{\ell=1}^*$ and $Z_{\ell=2}^*$ are given by

$$Z_{\ell=1}^* = \frac{1}{2} (Z_{^{[3]}O}^* - Z_{^{[3]}O}^{*T}), \quad (17)$$

$$Z_{\ell=2}^* = \frac{1}{2} (Z_{^{[3]}O}^* + Z_{^{[3]}O}^{*T}) - Z_{\ell=0}^*, \quad (18)$$

with the superscript T indicating the transpose matrix. We adopt a standard matricial norm (or matrix norm) [57] to quantify the respective weights of each ℓ component in Eq. (15). On average, we find that $Z_{\ell=1}^*$ is negligible (weight $\sim 0.03\%$), while the traceless symmetric term $Z_{\ell=2}^*$ (weight $\sim 3\%$) is well described by a diagonal matrix

$$Z_{\ell=2}^* = \begin{pmatrix} \lambda & 0 & 0 \\ 0 & \mu & 0 \\ 0 & 0 & -(\lambda + \mu) \end{pmatrix}. \quad (19)$$

By averaging over all $^{[3]}O$ atoms in our models and also keeping into account the three possible local bases for each O atom, we obtain the values $\lambda = -0.23$ and $\mu = 0.42$ with standard deviations of ≈ 0.1 . Due to the approximate trigonal symmetry $-(\lambda + \mu) \simeq \lambda$, which leads to the fact that the tensor Z^* can be regarded as isotropic in the xz plane. Hence, we adopt the following Born charge tensor for $^{[3]}O$ atoms, defined in their local reference frame:

$$Z_{^{[3]}O}^* = \begin{pmatrix} -2.1 & 0 & 0 \\ 0 & -1.5 & 0 \\ 0 & 0 & -2.1 \end{pmatrix}. \quad (20)$$

For fourfold-, fivefold-, and sixfold-coordinated Al atoms, the isotropic component ($\ell = 0$) accounts on average for 98.9%, 99.2%, and 99.6% of the norm of the Born charge tensors Z_{Al}^* , respectively. For fourfold-coordinated O atoms, the average isotropic component accounts for 98.5% of the Born charge, which is noticeably higher than for $^{[3]}O$ atoms (96.6%). It was found that the average isotropic dynamical charge of fourfold-coordinated O atoms $Z_{\text{iso}}^* = -1.95$, which is close to typical values given in the literature for O atoms in $\alpha\text{-Al}_2\text{O}_3$ [72]. Since the twofold-coordinated O atoms are rare [73] in am- Al_2O_3 (see Table I), we just retain here, for the sake of simplicity, their average isotropic Born charge ($Z_{\text{iso}}^* = -1.82$). All average isotropic charges of Al and O atoms to be used as parameters in the evaluation of IR spectra are given in Table IV.

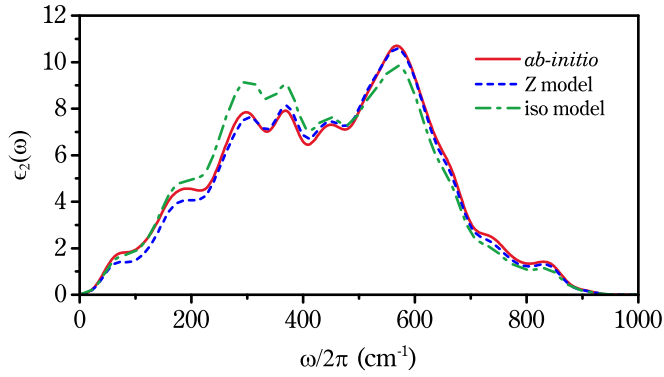


FIG. 7. The dielectric function $\epsilon_2(\omega)$ for model I calculated by using three alternative sets of Born effective charges: *ab initio* result (red, solid), *parametric* model (*Z* model) with values from Table IV (blue, dashed), and fully *isotropic* model (iso model) with $\bar{Z}_O^* = -1.91$ and $\bar{Z}_{Al}^* = 2.85$ (green, dot-dashed).

By taking advantage of Eqs. (15) and (19), and by assuming an isotropic charge for fourfold-coordinated O atoms and for Al atoms, it is possible to define a basic *parametric* model for the calculation of the Born charge tensors in am- Al_2O_3 . In Fig. 7, we show $\epsilon_2(\omega)$ spectra calculated with the parameters given in Table IV compared with the *ab initio* result. For convenience, the spectrum achieved with the *parametric* coupling is also compared with the result from a calculation with sole average *isotropic* charges, i.e., $\bar{Z}_O^* = -1.91$ and $\bar{Z}_{Al}^* = 2.85$ for all O and Al atoms, respectively. As we can see, the *isotropic* model is qualitatively correct, which is also implied by Sec. III C, but it overestimates the band at $\sim 350 \text{ cm}^{-1}$ and underestimates the band at 570 cm^{-1} , showing quite large discrepancies from 8% to 15% relative to the *parametric* model, which accurately reproduces the intensity of all the main features of the *ab initio* spectrum. The higher accuracy of the *parametric* model compared to the *isotropic* one is due to the fact that the *parametric* model accounts for the difference in coupling charges of ^{13}O atoms for *in-plane* and *out-of-plane* motions (the plane defined by its Al neighbors). As can be seen in Eq. (20), this difference amounts to $\sim 30\%$, with the coupling charge along the *out-of-plane* (normal) direction being smaller than along *in-plane* directions. As a result, in the $\epsilon_2(\omega)$ spectrum, the anisotropic Born charge of ^{13}O atoms [see Eq. (20)] leads to a lowering of the band intensity at $\sim 300\text{--}370 \text{ cm}^{-1}$ with respect to that at 570 cm^{-1} (see Fig. 7).

IV. DISCUSSION

IR spectroscopy is a common technique for analyzing am- Al_2O_3 films. In particular, absorption or transmission spectra are typically collected in the mid- and far-IR regions. These spectra are underlain by the dielectric function, the knowledge of which is essential for the correct description and interpretation of the features that appear in the experimental spectra.

Relying on the decomposition shown in Figs. 3 and 6, we associate the two main features of the $\epsilon_2(\omega)$ spectrum with the motions of ^{13}O atoms. In particular, the band peaking at $\sim 380 \text{ cm}^{-1}$ reflects the occurrence of oxygen motions in the direction normal to the plane of its Al neighbors (*out-of-plane* motions) in the OAl_3 units, while the band peaking

at $\sim 600\text{--}630 \text{ cm}^{-1}$ mainly results from *in-plane* motions of the same O atoms (i.e., from O-Al stretching vibrations). Hence, the $\epsilon_2(\omega)$ function (or equivalently, the absorption) of am- Al_2O_3 shows the presence of two main bands, and not of three bands, as, e.g., in other oxides glasses, such as vitreous silica [74]. This is clearly a consequence of the dominant occurrence of OAl_3 subunits in the structure of am- Al_2O_3 (see Table I). We note that the presence of triply coordinated O atoms (^{13}O) in am- Al_2O_3 was recently discovered by using a special NMR-spectroscopy study [17]. This study shows that these ^{13}O atoms carry detailed NMR characteristics that are peculiar to am- Al_2O_3 and differ substantially from those of ^{13}O atoms in crystalline counterparts, such as γ -alumina. In accordance with the remarks made in Ref. [17], we find here that in our models the dominant OAl_3 subunits contain one or two fivefold-coordinated Al atoms (see Table II), which do not occur in crystalline systems. Subunits containing threefold-coordinated atoms also critically affect the shape of the $\epsilon_2(\omega)$ spectrum in other materials, such as, e.g., amorphous Si_3N_4 , where nitrogen atoms are mostly threefold-coordinated with silicon atoms [69]. As in am- Al_2O_3 , the $\epsilon_2(\omega)$ spectrum in amorphous Si_3N_4 exhibits two bands, located at ~ 480 and $\sim 820 \text{ cm}^{-1}$ [69]. These bands are sharper than those of am- Al_2O_3 , which can be explained by the fact that the structure of amorphous Si_3N_4 is dominated by silicon-centered tetrahedra, while the structure of am- Al_2O_3 is more complex, with several competing types of Al-centered polyhedra.

Even if the $\epsilon_2(\omega)$ spectrum in am- Al_2O_3 might at first glance resemble that of α - Al_2O_3 , which consists of several sharp features located in the ranges $380\text{--}440$ and $570\text{--}635 \text{ cm}^{-1}$ [75], the origin of the vibrational modes at $\sim 380 \text{ cm}^{-1}$ in am- Al_2O_3 is essentially different. In α - Al_2O_3 all the O atoms are fourfold-coordinated, while the vast majority of O atoms in am- Al_2O_3 are threefold-coordinated, which leads to the appearance of a broad band peaking at $\sim 380 \text{ cm}^{-1}$ in the $\epsilon_2(\omega)$ spectrum and featuring oxygen motion in the direction normal to the plane of three Al neighbors. The modes at $\sim 380 \text{ cm}^{-1}$ in am- Al_2O_3 inevitably differ from the modes arising upon bending modes of single AlO_6 octahedra in α - Al_2O_3 [76], where there are no ^{13}O atoms. In fact, all bending modes of the AlO_4 , AlO_5 , and AlO_6 polyhedra present in am- Al_2O_3 should be considered, but a detailed analysis based on all vibrations of polyhedra is beyond the scope of this work. Nevertheless, the presence of structural motifs characteristic of the α - Al_2O_3 phase, i.e., edge-sharing polyhedra and sixfold Al polyhedra, in particular, can accidentally lead to a spatially local analogy between the vibrational modes of crystalline phases and the vibrational modes observed in the amorphous phase.

Among the transition alumina phases [15], θ -alumina features the largest fraction (50%) of AlO_4 tetrahedra and AlO_6 octahedra, and, rather similarly to the amorphous phase, it also features a remarkable fraction (66%) of ^{13}O atoms (OAl_3 units in θ -alumina are of the $\text{O}^{[4]}\text{Al}^{[6]}\text{Al}_2$ and $\text{O}^{[4]}\text{Al}_2^{[6]}\text{Al}$ kinds showing a degree of planarity of 0.96 and 0.99, respectively) and a rather similar density ($\sim 3.6 \text{ g/cm}^3$ [77]). IR-spectroscopy studies of transition alumina phases assign a doublet with features at ~ 330 and 370 cm^{-1} in the absorbance spectrum to the occurrence of the θ -alumina phase [76,78,79]. Considering that θ -alumina and am- Al_2O_3 have

some structural similarity, as noted above, one can conclude that vibrational modes around $\sim 330\text{ cm}^{-1}$ in θ -alumina [76] should have similar characteristics. In fact, in the present work we find (Figs. S3 and S4 in the Supplemental Material [47]) that in the frequency range $280\text{--}340\text{ cm}^{-1}$ the vibrational modes of the θ -alumina show significant *out-of-plane* motions of ^{16}O atoms. In our IR calculations (PBE-DFT), the highest frequency peak of the peculiar doublet is underestimated by about 40 cm^{-1} (i.e., 11%) [76,80]. We thus infer that the peak position ($\sim 320\text{ cm}^{-1}$) related to *out-of-plane* O motions, as found in our calculations (see Figs. 5 and 6), may suffer from a redshift of $\sim 40\text{ cm}^{-1}$ with respect to the experimental frequency. This further supports the assignment of the 370 cm^{-1} band in $\epsilon_2(\omega)$ to *out-of-plane* motions of ^{16}O atoms.

A comparison between the various IR spectra of the models discussed here does not allow one to estimate the concentration of fourfold-coordinated O atoms. However, based on Fig. 5, several considerations can be made. First, the Al-O bond-length distribution of model I is shifted towards longer bonds compared to other models. Since the distribution reflects the variety of structural motifs present in model I, the shift can be explained by an excessively frequent occurrence of fivefold- and sixfold-coordinated Al atoms, as well as of fourfold-coordinated O atoms, which leads to an increase in the average Al-O bond length (see Sec. III A). Second, the trend (see Fig. 4) that correlates the Al-O bond lengths and the stretching frequencies, together with the distributions of Al-O bond lengths (see Fig. 2), implies that, in the $\epsilon_2(\omega)$ spectrum of model I, the stretching bands will be redshifted compared with those of models II and III, thus explaining the lower frequency of the main peak (570 cm^{-1}) and rapid decay of $\epsilon_2(\omega)$ spectrum above $\sim 650\text{ cm}^{-1}$.

On the other hand, the *out-of-plane* oxygen band peaking at $\sim 320\text{ cm}^{-1}$ in model II is too sharp [see Fig. 5(b)], which probably indicates an excess of OAl_3 units in the model. Among the three models, the model that gives the values of $\epsilon_2(\omega)$ closest to the experiment in terms of the positions of the bands and the overall shape of the spectrum is model III. In terms of the global shape of the spectrum, however, we achieve the best description of $\epsilon_1(\omega)$, $\epsilon_2(\omega)$, and $-\text{Im}[1/\epsilon(\omega)]$ by averaging over all our models. This indicates that the set of models used in the present work is sufficiently representative of am- Al_2O_3 , although none of the adopted models provide such a good agreement individually. On the whole, as regards the intensities of the bands and the positions of the peaks, we have a better agreement between the calculated average IR spectra and those measured in this work compared to Ref. [21].

The averaged $\epsilon_1(\omega)$ spectrum shows a very strained and stretched S-like shape, reminiscent of the one in silica [81]. From the high-frequency limit of the calculated $\epsilon_1(\omega)$ we derive a refractive index $n = \sqrt{\epsilon_\infty}$ of ~ 1.7 , which is consistent with the upper values pertaining to very compact am- Al_2O_3 films [60]. In the low-frequency limit, we obtain for ϵ_0 a value of $\sim 10\text{--}11$, which belongs to the upper side of the typical experimental range $\sim 8\text{--}11$ (see Table III).

While the formation of am- Al_2O_3 is thermodynamically quite unfavorable, it can be stabilized by applying interface, surface, or bulk stress. Indeed, producing thin films and

nanoparticles was shown to be a successful approach to stabilize am- Al_2O_3 [7]. In the present study, the electron-beam deposition technique at extremely low deposition rate is used to prepare homogeneous, void-free am- Al_2O_3 as indicated by Tane *et al.* [82]. We note that other kinds of am- Al_2O_3 thin films, e.g., prepared by rf sputtering, are known to have a grainy structure, which consequently introduces a source of scattering that affects the recorded IR spectra, while ALD prepared films contain carbon and chlorine impurities, which are absent in high-quality electron-beam deposited alumina films. Furthermore, a background subtraction processing is crucial to obtain a correct dielectric function. In our study, a transmission spectrum of a blank Si substrate is subtracted, allowing one to calculate the dielectric function taking advantage of the absence of IR absorption in the substrate. The ability to avoid measuring the reflectance eliminates the need to correctly indicate the intensity of the reflectance, which is usually related to Au (see Ref. [21]), and in fact differs from the reflectance at the substrate interface, thereby introducing a systematic error. However, in the case of thin films, it is particularly challenging to extract the dielectric function through the Kramers-Kronig relations, because of the multiple reflections and inferences arising from light interaction at the film-substrate interfaces and grain boundaries. Additionally, systematic errors in reflectivity measurements can occur by choosing, storing, and measuring a suitable reference for the reflectivity measurements [83]. In this work, we demonstrate that using the iterative procedure developed in Ref. [49] is an efficient way for obtaining the dielectric function from a *single* transmission spectrum. The value of the dielectric function in the mid-IR range nicely follows the experimental data previously reported by Eriksson *et al.* [21], while in the far-IR range Eriksson's data show lower values. The origin of the discrepancy might arise from the processing method used to prepare the thin films [52]. The intensity in the $\epsilon_2(\omega)$ spectrum around 580 cm^{-1} measured in this work is larger compared with Eriksson's data. In light of our theoretical analysis, this may be attributed to a larger content of AlO_6 octahedra in the films used in the present work. Also, the films obtained by evaporation are not necessarily stoichiometric [21], which leads to some variability in the proportions of AlO_4 , AlO_5 , and AlO_6 polyhedra.

V. CONCLUSIONS

In this paper, we investigate the vibrational spectra, IR, and VDOS spectra in am- Al_2O_3 by means of first-principles calculations and experimental measurements. We validate our numerical results by carrying out a critical comparison of our calculated vibrational spectra with two sets of experimental data for the dielectric function of am- Al_2O_3 , taken from the literature [21] and measured in this work. In particular, the comparison between the latter data set and the dielectric function obtained through *ab initio* calculations results in an improved agreement with respect to the data by Eriksson *et al.* [21].

We show that the main features of the $\epsilon_2(\omega)$ spectrum peaking at $\sim 360\text{--}380$ and $\sim 600\text{--}630\text{ cm}^{-1}$ arise from the motions of threefold-coordinated O atoms, which form the vast majority of O atoms in am- Al_2O_3 . By using an

atomic decomposition analysis, we show that the oxygen motions at $\sim 370\text{ cm}^{-1}$ occur along a direction normal to the plane defined by the three Al nearest neighbors, i.e., *out-of-plane* O motions. At frequencies above $\sim 500\text{ cm}^{-1}$, Al-O stretching vibrations, which for threefold-coordinated O atoms correspond to *in-plane* motions, occur and underlie the broadband peaking at $\sim 600\text{--}630\text{ cm}^{-1}$. Al atoms and fourfold-coordinated O atoms give a fairly uniform contribution to the VDOS and $\epsilon_2(\omega)$ spectra in the frequency range of $300\text{--}700\text{ cm}^{-1}$ without manifesting specific features. Essentially, by conducting this comprehensive analysis we disclaim earlier hypotheses that relate the observed vibrational modes from ~ 200 to $\sim 400\text{ cm}^{-1}$ in am- Al_2O_3 to stretching vibrational modes in AlO_n ($n = 4, 5, \text{ and } 6$) polyhedra.

Finally, we demonstrate that the IR spectrum can be successfully modeled by assuming isotropic Born charges for Al atoms and fourfold-coordinated O atoms, while in the case of threefold-coordinated O atoms, the anisotropy of the Born charges can well be captured through the use of only two extra parameters in the local reference frame. The scope of the proposed Born charges model is quite wide, which allows modeling the spectra of much larger alumina models compared to *ab initio* ones, since it allows for a direct calculation of IR spectra requiring only the atomic configuration, vibra-

tional modes, and frequencies, i.e., obtained by using classical MD simulations.

ACKNOWLEDGMENTS

L.G. and A.M. acknowledge financing of the Slovenian Research Agency (ARRS) through the Research Core Funding No. P2-0412. A.M. also acknowledges ARRS support through Project No. J2-2498, and L.G. acknowledges support through the CEA-ARRS Project No. 0018. Y.L. acknowledges the financial support from the National Natural Science Foundation of China (22279013, 21872019). N.S.S. acknowledges support from the French government (ANR) through the national program Investments for the Future, Grant No. ANR-11-LABX022-01 (LabEx MMCD project). We acknowledge H. Momida (Osaka University) for providing us with models of Ref. [27]. We acknowledge EPFL for providing access to hpc facilities at EPFL (SCITAS) and I. Jerman from National Institute of Chemistry (Slovenia) for recording IR spectra. L.G. thanks N. Salles (CNR-IOM) for providing a θ -alumina supercell, J. Kurtovic for test calculations, and S. de Gironcoli (SISSA) for usage of computational resources at CINECA and useful discussions.

-
- [1] C.-C. Hung, L. Yu, N. Foroozani, S. Fritz, D. Gerthsen, and K. D. Osborn, Probing Hundreds of Individual Quantum Defects in Polycrystalline and Amorphous Alumina, *Phys. Rev. Appl.* **17**, 034025 (2022).
- [2] E. A. Scott, J. T. Gaskins, S. W. King, and P. E. Hopkins, Thermal conductivity and thermal boundary resistance of atomic layer deposited high-k dielectric aluminum oxide, hafnium oxide, and titanium oxide thin films on silicon, *APL Mater.* **6**, 058302 (2018).
- [3] J. Reuna, A. Aho, R. Isoaho, M. Raappana, T. Aho, E. Anttola, A. Hietalahti, A. Tukiainen, and M. Guina, Use of nanostructured alumina thin films in multilayer anti-reflective coatings, *Nanotechnology* **32**, 215602 (2021).
- [4] F. García Ferré, A. Mairov, L. Ceseracciu, Y. Serruys, P. Trocellier, C. Baumier, O. Kaïtasov, R. Brescia, D. Gastaldi, P. Vena, M. G. Beghi, L. Beck, K. Sridharan, and F. Di Fonzo, Radiation endurance in Al_2O_3 nanoceramics, *Sci. Rep.* **6**, 33478 (2016).
- [5] J. Robertson and B. Falabretti, Band offsets of high K gate oxides on III-V semiconductors, *J. Appl. Phys.* **100**, 014111 (2006).
- [6] Z. Zhao, D. Xiao, K. Chen, R. Wang, L. Liang, Z. Liu, I. Hung, Z. Gan, and G. Hou, Nature of five-coordinated Al in $\gamma\text{-Al}_2\text{O}_3$ revealed by ultra-high-field solid-state NMR, *ACS Central Sci.* **8**, 795 (2022).
- [7] A. Mavrič, M. Valant, C. Cui, and Z. M. Wang, Advanced applications of amorphous alumina: From nano to bulk, *J. Non-Cryst. Solids* **521**, 119493 (2019).
- [8] M. Fukuhara, T. Kuroda, F. Hasegawa, T. Hashida, E. Kwon, and K. Konno, Amorphous aluminum-oxide supercapacitors, *Europhys. Lett.* **123**, 58004 (2018).
- [9] A. Zaborowska, M. Clozel, E. Olivier, J. O'Connell, M. Vanazzi, F. Di Fonzo, A. Azarov, I. Jóźwik, M. Frelek-Kozak, R. Diduszko, J. H. Neethling, and J. Jagielski, Absolute radiation tolerance of amorphous alumina coatings at room temperature, *Ceram. Int.* **47**, 34740 (2021).
- [10] M. Valant, U. Luin, M. Fanetti, A. Mavrič, K. Vyshniakova, Z. Siketić, and M. Kalin, Fully transparent nanocomposite coating with an amorphous alumina matrix and exceptional wear and scratch resistance, *Adv. Funct. Mater.* **26**, 4362 (2016).
- [11] A. F. Harper, K. Iwanowski, M. C. Payne, and M. Simoncelli, Vibrational and thermal properties of amorphous alumina from first principles, [arXiv:2303.08637](https://arxiv.org/abs/2303.08637).
- [12] S. K. Lee, S. Y. Park, Y. S. Yi, and J. Moon, Structure and disorder in amorphous alumina thin films: Insights from high-resolution solid-state NMR, *J. Phys. Chem. C* **114**, 13890 (2010).
- [13] S. K. Lee, S. B. Lee, S. Y. Park, Y. S. Yi, and C. W. Ahn, Structure of Amorphous Aluminum Oxide, *Phys. Rev. Lett.* **103**, 095501 (2009).
- [14] N. Kim, R. Bassiri, M. M. Fejer, and J. F. Stebbins, The structure of ion beam sputtered amorphous alumina films and effects of Zn doping: High-resolution ^{27}Al NMR, *J. Non-Cryst. Solids* **405**, 1 (2014).
- [15] R. Lizárraga, E. Holmström, S. C. Parker, and C. Arrouvel, Structural characterization of amorphous alumina and its polymorphs from first-principles XPS and NMR calculations, *Phys. Rev. B* **83**, 094201 (2011).
- [16] R. Nakamura, M. Ishimaru, H. Yasuda, and H. Nakajima, Atomic rearrangements in amorphous Al_2O_3 under electron-beam irradiation, *J. Appl. Phys.* **113**, 064312 (2013).
- [17] S. K. Lee and S. Ryu, Probing of triply coordinated oxygen in amorphous Al_2O_3 , *J. Phys. Chem. Lett.* **9**, 150 (2018).
- [18] C. Shi, O. L. Alderman, D. Berman, J. Du, J. Neufeind, A. Tamalonis, J. R. Weber, J. You, and C. J. Benmore, The

- structure of amorphous and deeply supercooled liquid alumina, *Front. Mater.* **6**, 38 (2019).
- [19] H. Hashimoto, Y. Onodera, S. Tahara, S. Kohara, K. Yazawa, H. Segawa, M. Murakami, and K. Ohara, Structure of alumina glass, *Sci. Rep.* **12**, 516 (2022).
- [20] D. L. Cortie, M. J. Cyster, T. A. Ablott, C. Richardson, J. S. Smith, G. N. Iles, X. L. Wang, D. R. G. Mitchell, R. A. Mole, N. R. de Souza, D. H. Yu, and J. H. Cole, Boson peak in ultrathin alumina layers investigated with neutron spectroscopy, *Phys. Rev. Res.* **2**, 023320 (2020).
- [21] T. Eriksson, A. Hjortsberg, G. Niklasson, and C.-G. Granqvist, Infrared optical properties of evaporated alumina films, *Appl. Opt.* **20**, 2742 (1981).
- [22] T. Ohwaki and T. Onishi, Infrared absorption at longitudinal optical frequency in amorphous oxides and their mixtures, *Jpn. J. Appl. Phys.* **38**, L1191 (1999).
- [23] T. Maruyama and S. Arai, Aluminum oxide thin films prepared by chemical vapor deposition from aluminum acetylacetonate, *Appl. Phys. Lett.* **60**, 322 (1992).
- [24] Y. Chu, J. Bates, C. White, and G. Farlow, Optical dielectric functions for amorphous Al_2O_3 and $\gamma\text{-Al}_2\text{O}_3$, *J. Appl. Phys.* **64**, 3727 (1988).
- [25] J. Orosco and C. F. M. Coimbra, Optical response of thin amorphous films to infrared radiation, *Phys. Rev. B* **97**, 094301 (2018).
- [26] Z. Li, P. R. Wray, M. P. Su, Q. Tu, H. P. Andaraarachchi, Y. J. Jeong, H. A. Atwater, and U. R. Kortshagen, Aluminum oxide nanoparticle films deposited from a nonthermal plasma: Synthesis, characterization, and crystallization, *ACS Omega* **5**, 24754 (2020).
- [27] H. Momida, T. Hamada, Y. Takagi, T. Yamamoto, T. Uda, and T. Ohno, Theoretical study on dielectric response of amorphous alumina, *Phys. Rev. B* **73**, 054108 (2006).
- [28] P. Vashishta, R. K. Kalia, A. Nakano, and J. P. Rino, Interaction potentials for alumina and molecular dynamics simulations of amorphous and liquid alumina, *J. Appl. Phys.* **103**, 083504 (2008).
- [29] G. Gutiérrez, E. Menéndez-Proupin, C. Loyola, J. Peralta, and S. Davis, Computer simulation study of amorphous compounds: Structural and vibrational properties, *J. Mater. Sci.* **45**, 5124 (2010).
- [30] W. Li, Y. Ando, and S. Watanabe, Effects of density and composition on the properties of amorphous alumina: A high-dimensional neural network potential study, *J. Chem. Phys.* **153**, 164119 (2020).
- [31] B. Begemann, J. Dorschner, T. Henning, H. Mutschke, J. Gürtler, C. Kömpe, and R. Nass, Aluminum oxide and the opacity of oxygen-rich circumstellar dust in the 12-17 micron range, *Astrophys. J.* **476**, 199 (1997).
- [32] W. Kübler, Properties of Al_2O_3 thin films prepared by ion-assisted evaporation, *Thin Solid Films* **199**, 247 (1991).
- [33] K. M. Eisele, Charge storage and stoichiometry in electron beam evaporated alumina, *J. Electrochem. Soc.* **122**, 148 (1975).
- [34] K. Shamala, L. Murthy, and K. N. Rao, Studies on optical and dielectric properties of Al_2O_3 thin films prepared by electron beam evaporation and spray pyrolysis method, *Mater. Sci. Eng.: B* **106**, 269 (2004).
- [35] V. Mikhaelashvili, Y. Betzer, I. Prudnikov, M. Orenstein, D. Ritter, and G. Eisenstein, Electrical characteristics of metal-dielectric-metal and metal-dielectric-semiconductor structures based on electron beam evaporated Y_2O_3 , Ta_2O_5 and Al_2O_3 thin film, *J. Appl. Phys.* **84**, 6747 (1998).
- [36] J. P. Perdew, K. Burke, and M. Ernzerhof, Generalized Gradient Approximation Made Simple, *Phys. Rev. Lett.* **77**, 3865 (1996).
- [37] We used the pseudopotential files 0.pbe-mt.UPF, Al.pbe-rrkj.UPF as available from the QE website <http://www.quantum-espresso.org>.
- [38] For the purposes of the present work, which are the description of the local mode symmetry and clarification the origin of the main IR bands, frequency shifts ($\sim 10\text{ cm}^{-1}$) related to the choice of the exchange-correlation functional [80] are minor issues not affecting the conclusion of the present paper.
- [39] D. Colleoni, G. Miceli, and A. Pasquarello, Band alignment and chemical bonding at the GaAs/ Al_2O_3 interface: A hybrid functional study, *Appl. Phys. Lett.* **107**, 211601 (2015).
- [40] P. Giannozzi, S. Baroni, N. Bonini, M. Calandra, R. Car, C. Cavazzoni, D. Ceresoli, G. L. Chiarotti, M. Cococcioni, I. Dabo, A. Dal Corso, S. de Gironcoli, S. Fabris, G. Fratesi, R. Gebauer, U. Gerstmann, C. Gougousis, A. Kokalj, M. Lazzeri, L. Martin-Samos *et al.*, QUANTUM ESPRESSO: a modular and open-source software project for quantum simulations of materials, *J. Phys.: Condens. Matter* **21**, 395502 (2009).
- [41] P. Lamparter and R. Kniep, Structure of amorphous Al_2O_3 , *Phys. B: Condens. Matter* **234-236**, 405 (1997).
- [42] Z. Guo, F. Ambrosio, and A. Pasquarello, Oxygen defects in amorphous Al_2O_3 , *Mater. Cloud Arch.* **2019**, 0026/v1 (2019).
- [43] M. Matsui, Molecular dynamics study of the structures and bulk moduli of crystals in the system $\text{CaO-MgO-Al}_2\text{O}_3\text{-SiO}_2$, *Phys. Chem. Miner.* **23**, 345 (1996).
- [44] H. Momida, T. Hamada, and T. Ohno, First-principles study of dielectric properties of amorphous high-k materials, *Jpn. J. Appl. Phys.* **46**, 3255 (2007).
- [45] T. F. Willems, C. H. Rycroft, M. Kazi, J. C. Meza, and M. Haranczyk, Algorithms and tools for high-throughput geometry-based analysis of crystalline porous materials, *Microporous Mesoporous Mater.* **149**, 134 (2012).
- [46] P. Hung and L. Vinh, Local microstructure of liquid and amorphous Al_2O_3 , *J. Non-Cryst. Solids* **352**, 5531 (2006).
- [47] See Supplemental Material at <http://link.aps.org/supplemental/10.1103/PhysRevMaterials.7.045604> for further details on thin film characterization, and on the calculation of IR active modes in θ -alumina and of participation ratio in am- Al_2O_3 .
- [48] H. A. Al-Abadleh and V. Grassian, FT-IR study of water adsorption on aluminum oxide surfaces, *Langmuir* **19**, 341 (2003).
- [49] P. A. Gerakines and R. L. Hudson, A modified algorithm and open-source computational package for the determination of infrared optical constants relevant to astrophysics, *Astrophys. J.* **901**, 52 (2020).
- [50] The first-principles relaxation of models II and III with PBE, as compared to the original LDA configurations from Momida [27] (and named there as model G and model H, respectively), shows a tendency to slightly increase the number of fivefold- and sixfold-coordinated Al atoms and of the number of fourfold-coordinated O atoms by decreasing the number of fourfold-coordinated Al atoms and twofold-coordinated O atoms.
- [51] J. Cui, M. G. Kast, B. A. Hammann, Y. Afriyie, K. N. Woods, P. N. Plassmeyer, C. K. Perkins, Z. L. Ma, D. A. Keszler, C. J. Page, S. W. Boettcher, and S. E. Hayes, Aluminum oxide thin

- films from aqueous solutions: Insights from solid-state nmr and dielectric response, *Chem. Mater.* **30**, 7456 (2018).
- [52] S. K. Lee and C. W. Ahn, Probing of 2 dimensional confinement-induced structural transitions in amorphous oxide thin film, *Sci. Rep.* **4**, 1 (2014).
- [53] A. Kokalj, XCrySDen—a new program for displaying crystalline structures and electron densities, *J. Mol. Graphics Modell.* **17**, 176 (1999).
- [54] R. J. Bell and P. Dean, The structure of vitreous silica: Validity of the random network theory, *Philos. Mag.* **25**, 1381 (1972).
- [55] N. S. Shcheblanov, L. Giacomazzi, M. E. Povarnitsyn, S. Kohara, L. Martin-Samos, G. Mountjoy, R. J. Newport, R. C. Haworth, N. Richard, and N. Ollier, Vibrational and structural properties of P₂O₅ glass: Advances from a combined modeling approach, *Phys. Rev. B* **100**, 134309 (2019).
- [56] M. F. Thorpe and S. W. de Leeuw, Coulomb effects in disordered solids, *Phys. Rev. B* **33**, 8490 (1986).
- [57] A. Pasquarello and R. Car, Dynamical Charge Tensors and Infrared Spectrum of Amorphous SiO₂, *Phys. Rev. Lett.* **79**, 1766 (1997).
- [58] M. E. Povarnitsyn, N. S. Shcheblanov, D. S. Ivanov, V. Y. Timoshenko, and S. M. Klimentov, Vibrational Analysis of Silicon Nanoparticles using Simulation and Decomposition of Raman Spectra, *Phys. Rev. Appl.* **14**, 014067 (2020).
- [59] P. Umari and A. Pasquarello, Infrared and raman spectra of disordered materials from first principles, *Diam. Relat. Mater.* **14**, 1255 (2005).
- [60] S.-M. Lee, D. G. Cahill, and T. H. Allen, Thermal conductivity of sputtered oxide films, *Phys. Rev. B* **52**, 253 (1995).
- [61] B. Segda, M. Jacquet, and J. Besse, Elaboration, characterization and dielectric properties study of amorphous alumina thin films deposited by r.f. magnetron sputtering, *Vacuum* **62**, 27 (2001).
- [62] E. Gusev, E. Cartier, D. Buchanan, M. Gribelyuk, M. Copel, H. Okorn-Schmidt, and C. D'emic, Ultrathin high-k metal oxides on silicon: processing, characterization and integration issues, *Microelectron. Eng.* **59**, 341 (2001).
- [63] M. T. Aguilar-Gama, E. Ramírez-Morales, Z. Montiel-González, A. Mendoza-Galván, M. Sotelo-Lerma, P. Nair, and H. Hu, Structure and refractive index of thin alumina films grown by atomic layer deposition, *J. Mater. Sci.: Mater. Electron.* **26**, 5546 (2015).
- [64] F. Evangelisti, M. Stiefel, O. Guseva, R. P. Nia, R. Hauert, E. Hack, L. P. Jeurgens, F. Ambrosio, A. Pasquarello, P. Schmutz, and C. Cancellieri, Electronic and structural characterization of barrier-type amorphous aluminium oxide, *Electrochim. Acta* **224**, 503 (2017).
- [65] L. Parfitt, M. Goldiner, J. W. Jones, and G. S. Was, Residual stresses in amorphous alumina films synthesized by ion beam assisted deposition, *J. Appl. Phys.* **77**, 3029 (1995).
- [66] P. Umari and A. Pasquarello, Polarizability and dielectric constant in density-functional supercell calculations with discrete k-point samplings, *Phys. Rev. B* **68**, 085114 (2003).
- [67] T. Eriksson, A. Hjortsberg, and C. Granqvist, Solar absorptance and thermal emittance of Al₂O₃ films on Al: A theoretical assessment, *Solar Energy Mater.* **6**, 191 (1982).
- [68] The experimental data of Refs. [21,67] have been digitized using the software Engauge Digitizer v.10.10. For the $\epsilon_2(\omega)$ function, we find peak positions at 378 and 627 cm⁻¹ with an estimated position error of ~2.5 cm⁻¹.
- [69] L. Giacomazzi and P. Umari, First-principles investigation of electronic, structural, and vibrational properties of α -Si₃N₄, *Phys. Rev. B* **80**, 144201 (2009).
- [70] F. Galeener and G. Lucovsky, Longitudinal Optical Vibrations in Glasses: GeO₂ and SiO₂, *Phys. Rev. Lett.* **37**, 1474 (1976).
- [71] L. Giacomazzi, P. Umari, and A. Pasquarello, Vibrational spectra of vitreous germania from first-principles, *Phys. Rev. B* **74**, 155208 (2006).
- [72] R. Heid, D. Strauch, and K.-P. Bohnen, *Ab initio* lattice dynamics of sapphire, *Phys. Rev. B* **61**, 8625 (2000).
- [73] O. A. Dicks, J. Cottom, A. L. Shluger, and V. V. Afanas'ev, The origin of negative charging in amorphous Al₂O₃ films: the role of native defects, *Nanotechnology* **30**, 205201 (2019).
- [74] L. Giacomazzi and A. Pasquarello, Vibrational spectra of vitreous SiO₂ and vitreous GeO₂ from first principles, *J. Phys.: Condens. Matter* **19**, 415112 (2007).
- [75] M. Schubert, T. E. Tiwald, and C. M. Herzinger, Infrared dielectric anisotropy and phonon modes of sapphire, *Phys. Rev. B* **61**, 8187 (2000).
- [76] A. Boumaza, L. Favaro, J. Lédion, G. Sattonnay, J. Brubach, P. Berthet, A. Huntz, P. Roy, and R. Tétot, Transition alumina phases induced by heat treatment of boehmite: An X-ray diffraction and infrared spectroscopy study, *J. Solid State Chem.* **182**, 1171 (2009).
- [77] H.-C. Kao and W.-C. Wei, Kinetics and microstructural evolution of heterogeneous transformation of θ -alumina to α -alumina, *J. Am. Ceram. Soc.* **83**, 362 (2000).
- [78] G. A. Dorsey, Far infrared absorption of hydrous and anhydrous aluminas, *Anal. Chem.* **40**, 971 (1968).
- [79] P. Tarte, Infra-red spectra of inorganic aluminates and characteristic vibrational frequencies of AlO₄ tetrahedra and AlO₆ octahedra, *Spectrochim. Acta Part A* **23**, 2127 (1967).
- [80] R. Demichelis, B. Civalleri, M. Ferrabone, and R. Dovesi, On the performance of eleven DFT functionals in the description of the vibrational properties of aluminosilicates, *Int. J. Quantum Chem.* **110**, 406 (2010).
- [81] L. Giacomazzi, P. Umari, and A. Pasquarello, Medium-range structure of vitreous SiO₂ obtained through first-principles investigation of vibrational spectra, *Phys. Rev. B* **79**, 064202 (2009).
- [82] M. Tane, S. Nakano, R. Nakamura, H. Ogi, M. Ishimaru, H. Kimizuka, and H. Nakajima, Nanovoid formation by change in amorphous structure through the annealing of amorphous Al₂O₃ thin films, *Acta Mater.* **59**, 4631 (2011).
- [83] J. M. Bennett and E. J. Ashley, Infrared reflectance and emittance of silver and gold evaporated in ultrahigh vacuum, *Appl. Opt.* **4**, 221 (1965).